



# 1. Introduction

Organic photovoltaic (OPV) energy conversion is a promising option among next generation renewable and sustainable energy technologies for a low-carbon energy future.<sup>1–3</sup> OPV has shown promising potential for various applications, such as indoor photovoltaics (PV),<sup>4–6</sup> semi-transparent solar windows,<sup>7,8</sup> PV greenhouses,<sup>9</sup> and off-grid power supply.<sup>10</sup> Recent OPV devices based on non-fullerene acceptors (NFAs) have demonstrated certified power conversion efficiencies (PCEs) exceeding 19% in a single junction configuration,<sup>11</sup> approaching the efficiencies observed in inorganic semiconductor PV technologies such as crystalline silicon and perovskite solar cells, and far higher than values thought attainable in OPV when using fullerene derivatives as the electron-acceptors.<sup>12</sup> The startling progress led by NFAs can be attributed to various advantages over fullerene derivatives, such as band-gap tunability, sharp absorption onset, high emission, high absorption, and low energy losses.<sup>13–15</sup> Among these advantages, the absorption strength of state-of-the-art NFAs is particularly outstanding, as exemplified in Fig. 1c (a detailed list of chemical names and nomenclatures is provided in Note S1, ESI†).<sup>16</sup> For instance, Y6 shows a maximum extinction coefficient ( $\kappa_{\max}$ ) over 1.5 in the visible part of the electromagnetic spectrum, as compared to less than 0.75 for fullerene derivatives (PC61BM and PC71BM). A high extinction coefficient increases the chance of high quantum efficiency and photogenerated current density, and makes it possible to fabricate highly absorbing OPV films with just a few tens of nanometre-thick photoactive layers. In comparison with workhorse fullerene acceptors, OPV devices based on highly absorbing NFAs could be made comparably thinner than the former, which exponentially raises the output power per weight (*i.e.* the specific weight in  $\text{W g}^{-1}$ ) of OPV devices<sup>17</sup> and might be an effective route toward lower production costs (as less material could be employed to achieve an equivalent PCE) and even increase device thermal stability.<sup>18</sup> Moreover, through detailed balance between photon absorption and emission,<sup>19,20</sup> high absorption strength in principle should lead to high emission from the NFAs, while strong NFA emission is believed to be a key reason for NFA-based OPVs to possess low nonradiative voltage losses.<sup>21–25</sup> Despite the clear advantage of strong photo-absorption of NFAs over fullerene derivatives, the phenomenon has attracted much less attention than other properties of NFAs.<sup>21–23,25–28</sup> Conceptually, symmetry rules (*i.e.*, the Laporte rule) can explain the qualitative difference between NFAs and fullerene derivatives in terms of absorption strength, yet such rules cannot predict differences in absorption strength among structures for which the lowest transitions are symmetry allowed. The features empirically and theoretically proposed<sup>29,30</sup> to lead to strong absorption in  $\pi$ -conjugated polymers are molecular stiffness, linearity, extended  $\pi$ -conjugation and large molecular size. It is therefore of interest to establish whether the same (or other) molecular features are quantitatively associated or not with increased absorption strength in NFAs, while seeking molecular design rules to drive absorption and performance higher in new molecules.

Excited state calculations based on quantum chemistry methods, such as time-dependent density functional theory

(TDDFT),<sup>8,29,31–33</sup> Hartree–Fock method,<sup>34</sup> *ab initio* Monte Carlo method,<sup>35</sup> second order Møller–Plesset theory (MP2),<sup>36</sup> and coupled cluster method,<sup>37</sup> have been applied to predict the electronic and optical properties of molecules. Among them, TDDFT is the most widely applied method for excited state calculations, and has shown reasonable accuracy in calculating and predicting the trends in absorption strength of organic molecules,<sup>29,31</sup> as also demonstrated in this work. However, the rapid scaling of computation time with molecular size has been the real obstacle limiting the applicability of TDDFT for excited state calculations on molecules with hundreds of atoms. Given the size and diverse structure of modern NFAs, faster and more efficient methods are therefore needed to establish the relationship between excited-state and molecular properties in NFAs.

The emergence of artificial intelligence (AI) has made it possible to study quantitative structure–property relationships (QSPRs) in molecules with massively improved computational efficiency. As the most popular branch of AI, machine-learning (ML) has attracted much attention in materials science over the last decade, and has been widely applied for material property prediction and material discovery.<sup>38–41</sup> Recently, ML has also gained popularity in OPV scenarios,<sup>42–52</sup> yet existing ML studies related to OPVs have been primarily focused either on the energetics<sup>42,43,53–56</sup> or directly on PCE,<sup>42,48,57–64</sup> with little attention paid to the absorption strength of the photoactive materials.<sup>65,66</sup> Moreover, there are no ML studies explicitly focused on the absorption strength of NFAs beyond the identification of moieties of frequent appearance in highly absorbing molecules.<sup>42</sup> However, QSPR and ML models have been successfully applied to investigate the absorption strength of fluorophores or dyes typically employed in bioimaging, showing encouraging results.<sup>30,67,68</sup> Therefore, it is appealing to apply ML methods in combination with QSPR models to investigate the origin of the large absorption strength in state-of-the-art NFAs.

Here, we present an experimental, TDDFT, QSPR, statistical and ML study of the absorption strength of NFAs to identify the key chemical and structural features that lead to high optical absorption in state-of-the-art NFAs. We exploit a database of nearly 500 unique organic molecules (or 3500 calculations) generated using DFT and TDDFT over several years. We obtain good quantitative agreement between TDDFT calculations of absorption strength and experimental values for state-of-the-art NFAs and fullerenes, which supports the use of TDDFT results for further statistical and QSPR modelling. Accordingly, we extract molecular information from the DFT-optimized geometries by computing nearly 6000 molecular descriptors and first looking for correlations with the absorption strength. The strongest correlations are found between experimentally measured maximum molar extinction coefficient ( $\epsilon_{\text{d,max}}$ ) and two main molecular descriptors from calculations:  $\lambda_{1,p}$  and C2SP2, which describe the size of the molecule in the direction of maximal atomic polarizability, and the number of  $\text{sp}^2$  hybridized carbon atoms that are bound to two other carbons (C2), respectively. These quantities can be related to a few key material features leading to high absorption strength: linearity,



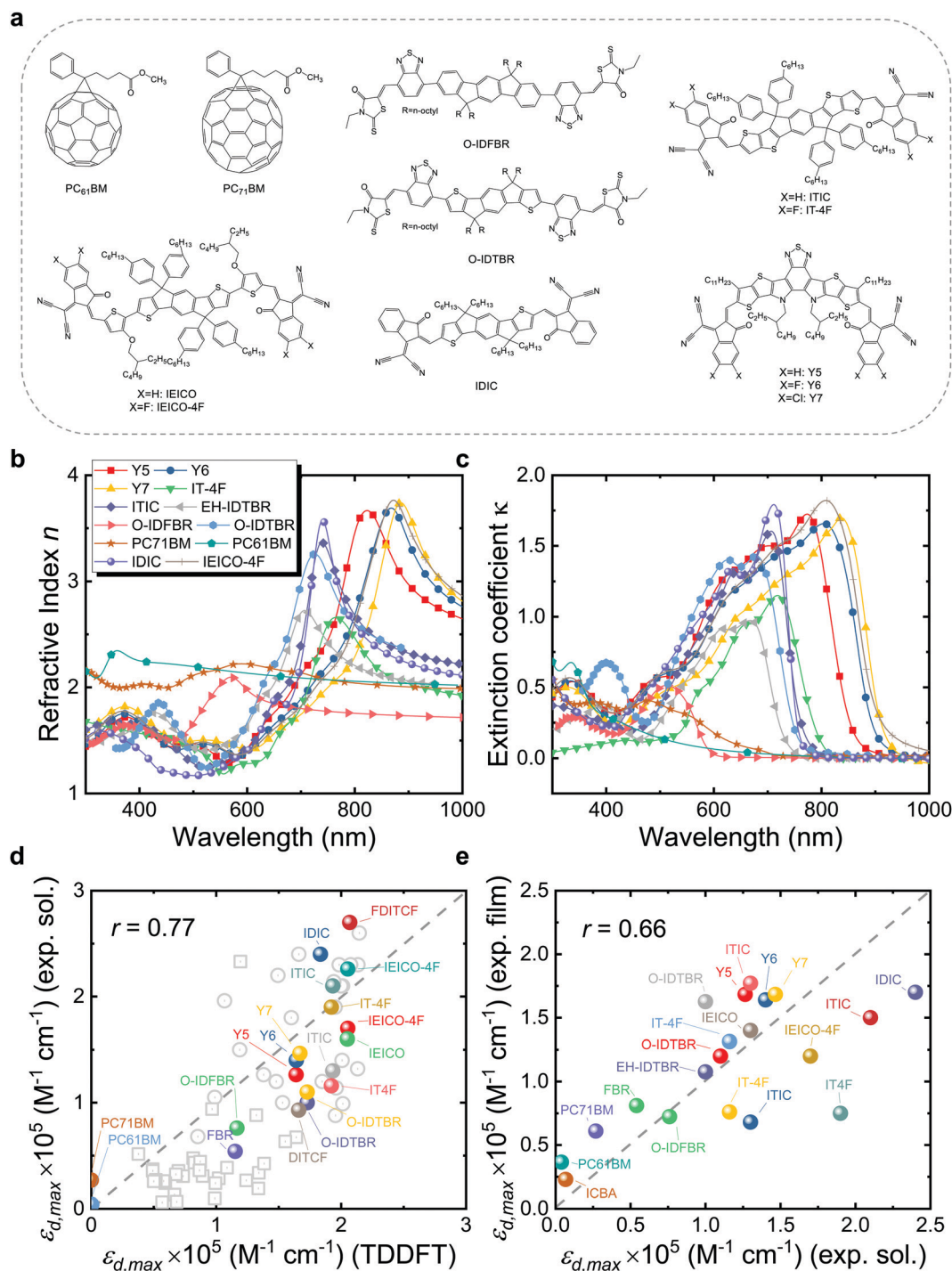


**Fig. 1** (a) Molecular structures of typical organic acceptors, including PC61BM, PC71BM, O-IDFBR, O-IDTBR, ITIC, IT-4F, IDIC, IEICO, IEICO-4F, Y5, Y6, and Y7. (b) Refractive index and (c) extinction coefficient of a larger set of typical organic acceptor thin films measured using VASE. (d) Experimental  $\epsilon_{d,max}$  in solution versus calculated  $\epsilon_{d,max}$  in vacuum using TDDFT of a set of  $\sim 80$   $\pi$ -conjugated molecules. (e) Estimated experimental  $\epsilon_{d,max}$  in film (solid state) versus that in solution using eqn (3). Panel (d) contains a subset of well-known NFA molecules that are highlighted in colour. All TDDFT results in panel (d) were performed using the functional B3LYP and basis set 6-311+G(d,p), except for the ones (grey squares) taken from ref. 69 that are based on the LRC-wPBEh functional and 6-311+G(d) basis set. We also note here that the side chains of molecules are replaced by H atoms or methyl groups in the calculations as they are computationally expensive and do not contribute to the  $\pi$ -conjugation, hence electronic transitions.<sup>29</sup> The experimental data of  $\epsilon_{d,max}$  in film are converted from maximum values of extinction coefficients shown in panel (c) using eqn (3), while solution data are collected from literature, noting that different values may be present for the same material as retrieved from different sources. Grey dashed lines indicate the perfect match between x and y axis. The data required for generating panels (d) and (e) in this figure are presented in the ESI.†



planarity, and extension of the  $\pi$ -conjugation in the form of fused and closed-ring moieties, in good agreement with previous ML reports on fluorophores and dyes.<sup>30</sup> We further identify several moieties and paired combinations thereof that are frequently found in highly absorbing NFAs, corresponding to thieno[3,2-*b*]thiophene (TT), thiophene (T), 2-(5,6-difluoro-3-oxo-2,3-dihydro-1*H*-inden-1-ylidene)malononitrile (2FIC), 2-(3-oxo-2,3-dihydro-1*H*-inden-1-ylidene)malononitrile (IC) and indaceno [1,2-*b*:5,6-*b'*]dithiophene (IDT). These form a catalogue of molecular design rules to further enhance the absorption strength of organic  $\pi$ -conjugated molecules, such as next-generation NFAs. We then train and test an ensemble learning method, namely a random decision forest (RF), to predict  $\epsilon_{d,\max}$  and provide further information about the most important features in the modelling of absorption strength in organic  $\pi$ -conjugated molecules. Finally, we explore the possibility to predict  $\epsilon_{d,\max}$  while using a cheaper molecular geometry optimization method based on semiempirical extended tight-binding (xTB) Hamiltonians instead of the expensive DFT approach. We do so by training a RF with our TDDFT database and proving its predictive properties in terms of  $\epsilon_{d,\max}$  when interpolated using xTB-optimized geometries. This approach shows application potential in high-throughput screening studies in combination with generative molecular models.

## 2. Results and discussion

### 2.1. Experimental validation of calculated absorption strength using TDDFT

Quantifying how well the TDDFT derived excited state properties agree with the experimental measurements in terms of absorption strength is of utmost importance to validate our theoretical calculations and support further conclusions extracted thereof. Accordingly, we first evaluate the agreement between TDDFT calculations and experimental data in terms of the absorption strength. We compare the absorption strength of a broad catalogue (~10 molecules) of NFA molecules and widely studied fullerene derivatives (PC61BM and PC71BM, with their molecular structures shown in Fig. 1a) as obtained from TDDFT calculations, with a variety of optical measurements in both solution and solid state. For the most representative NFAs examined, we verify that their frontier molecular orbital energy levels as retrieved from TDDFT calculations are properly aligned, relative to those of a set of common polymer donors, for the NFAs to act as electron acceptor in a bulk heterojunction blend with those donors (Fig. S1, ESI†). The measured refractive index ( $n$ ) and extinction coefficient ( $\kappa$ ) of those molecules in thin film obtained using our variable-angle spectroscopic ellipsometry (VASE) measurements are shown in Fig. 1b and c. Solution state data shown in Fig. 1d and e are collected from a variety of literature references as detailed in the ESI.†<sup>1</sup>

As a metric for absorption strength, we initially consider several candidates such as the oscillator strength ( $f_{\text{osc}}$ ), the absorption coefficient ( $\alpha$ ) or the imaginary part of the dielectric function ( $\epsilon_2$ ). In this work, we eventually focus on the maximum

molar extinction coefficient ( $\epsilon_{d,\max}$ ,  $\text{M}^{-1} \text{cm}^{-1}$ ) of NFAs as it shows the best agreement between experimental and theoretical data, as we demonstrate below.  $\epsilon_{d,\max}$  constitutes a typical experimental measurement in solution that can also be accessed from myriad literature references. Note that the usual calculations based on single molecules using TDDFT cannot account for solid state effects as they are performed for isolated molecules in vacuum or surrounded by an isotropic medium (such as a solvent using the polarizable-continuum-solvent-model, PCM, Fig. S2, ESI†). The derivation of the theoretical  $\epsilon_d$  is provided in the Methods section, which results in a mathematical expression for  $\epsilon_{d,\max}$  as

$$\epsilon_{d,\max} = 10 \log_{10}(e) N_A \frac{2\pi e \hbar}{3\epsilon_0 m_0 n_r c} f_{\text{osc,max}} \frac{1}{\sigma \sqrt{2\pi}}, \quad (1)$$

where  $N_A$  is the Avogadro constant,  $e$  the elementary charge,  $\hbar$  the reduced Planck constant,  $\epsilon_0$  the vacuum permittivity,  $m_0$  the electron mass,  $n_r$  is the refractive index in solution (assumed to be 1.3 of a common organic solvent throughout this study), and  $c$  the speed of light.  $f_{\text{osc,max}}$  is the oscillator strength of the strongest transition among the calculated states within the visible-IR part of the spectrum, and  $E_{\text{max}}$  is the energy of that transition. The brightest transition is very often the lowest-energy transition in commonly used  $\pi$ -conjugated molecules.<sup>29</sup> We note here that the delta function in eqn (17) is replaced with a Gaussian distribution function with a peak intensity of  $\frac{1}{\sigma \sqrt{2\pi}}$ , where  $\sigma$  is the Gaussian width and assumed to be 0.1 eV for a common organic pi-conjugated molecule.

The experimental  $\epsilon_{d,\max}$  from solution can be obtained using the optical density (OD) measurements performed using UV-visible spectroscopy, *via*

$$\epsilon_{d,\max} = \frac{\text{OD}_{\max}}{\rho d}, \quad (2)$$

where  $\text{OD}_{\max}$  is the maximum optical density,  $\rho$  is the molar concentration (M), and  $d$  the light path length of the cuvette (cm). Similarly, the experimental  $\epsilon_{d,\max}$  from film can be estimated assuming a mass concentration  $\rho_M$  in the film of  $1000 \text{ g L}^{-1}$  (as a typical value for conjugated polymers and small molecules),<sup>29</sup> either from the maximum absorption coefficient  $\alpha_{\text{cm,max}}$  ( $\text{cm}^{-1}$ ) or extinction coefficient ( $\kappa_{\text{max}}$ ) (Fig. 1c), *via*

$$\epsilon_{d,\max} = \log_{10}(e) \alpha_{\text{cm,max}} \frac{M_w}{\rho_M} = \log_{10}(e) \frac{4\pi \kappa_{\text{max}} M_w}{\lambda_{\text{max}} \rho_M}, \quad (3)$$

where  $M_w$  is the molecular weight in  $\text{g mol}^{-1}$ , and  $\lambda_{\text{max}}$  the wavelength at  $\kappa_{\text{max}}$  in centimetre.

Fig. 1d presents the results of the comparison between experimental  $\epsilon_{d,\max}$  in solution and theoretical  $\epsilon_{d,\max}$  calculated from single molecules using TDDFT in vacuum. A brief discussion of the solvent effect on the absorption strength and the reasons why we choose a vacuum medium are provided in Fig. S2 (ESI†). Despite the scattering of data points, we observe the occurrence of a monotonic relationship between solution and calculated  $\epsilon_{d,\max}$  with a Pearson correlation coefficient ( $r$ ) of 0.77. Interestingly, such correlation is no longer observed when





quantifying the absorption strength in terms of  $\alpha_{\max}$  neither when adding further data points from literature on  $\pi$ -conjugated fluorophores to our statistical analysis (Fig. S3a (ESI<sup>†</sup>),  $r = 0.30$ ), which is believed to be caused by the differences in molecular weight; in that case, only  $\epsilon_{d,\max}$  is found to follow a monotonic trend (Fig. S3b, ESI<sup>†</sup>). Some of the material assumptions on refractive index and density required to obtain  $\alpha_{\max}$  values might be responsible for the observed mismatch. It is worth noting that, expectedly, the correlation between solid state (film) and solution ( $r = 0.66$ , Fig. 1e) or calculated  $\epsilon_{d,\max}$  ( $r = 0.61$ , Fig. 1e) is not as good as that from solution data *versus* calculated  $\epsilon_{d,\max}$  ( $r = 0.77$ , Fig. 1d, neither for  $\alpha_{\max}$  as shown in Fig. S4, ESI<sup>†</sup>). Such discrepancy is attributed to solid-state effects such as aggregation effects,<sup>15</sup> intermolecular orientation,<sup>70,71</sup> and side chain interactions,<sup>72</sup> which are not considered in single molecule excited state calculations.<sup>29</sup> The observed trend that a highly absorbing material in solution will produce highly absorbing films is, nonetheless, generally valid and thus solution data are relevant for devices. Since the NFAs analysed here have a rather similar number of  $\pi$ -electrons ( $n_{\pi}$ ), the corresponding  $\epsilon_{d,\max}$  per  $\pi$ -electron (Fig. S6, ESI<sup>†</sup>) shows a similar trend as that in Fig. 1d, e, and Fig. S4 (ESI<sup>†</sup>). Despite the simplicity of single molecule excited state calculations, these data show that using TDDFT calculations of the excited state to deliver  $\epsilon_{d,\max}$  can provide a reasonably good approximation to experimental measurements. Moreover, dealing with TDDFT calculations gives us room to correlate key molecular properties, such as molecular size and shape (aspect ratio), linearity, planarity, grafted side chain positions, or functional groups, to the absorption strength using molecular descriptors. These observations provide a foundation from molecular structures to identify the origin and further extend the high optical extinction of NFAs through chemical design rules, as we show in the upcoming sections.

## 2.2. Statistical analysis of the TDDFT absorption strength dataset

The experimental validation of the TDDFT calculations in NFAs supports the use of such results to build an extended database of optimized molecular geometries and excited state properties. The dataset is built by collecting thousands of molecular geometries generated over the last years in our group, making up a total of 3515 calculations on small molecules and oligomers. The distribution of number of atoms in a molecule is shown in Fig. S7 (ESI<sup>†</sup>) with a majority lying between 50 and 100 atoms. This database is sufficiently diverse to allow us to detect correlations and chemical/structural design rules that could explain and/or further enhance optical absorption in conjugated small molecules.

**2.2.1. Correlation analysis of molecular descriptors.** In the simplest statistical analysis of our TDDFT database, we look for correlations of the absorption strength with respect to a catalogue of molecular descriptors. First, as described in Note S2 (ESI<sup>†</sup>), we filter the pristine TDDFT database by identifying duplicate molecules (in terms of molecular weight) and selecting the lowest energy conformer (*i.e.*, optimized geometries in the

ground state) among them. As a result, the curated TDDFT database employed in this work consists of 479  $\pi$ -conjugated small molecules and oligomers with a distribution of moieties shown in Fig. S9 (ESI<sup>†</sup>).

Then, we introduce several target features related with absorption strength, starting from the maximum oscillator strength of any calculated transition ( $f_{\max}$ ); the maximum oscillator strength of any transition in the visible electromagnetic window (herein constrained between 300–1200 nm or 1–4 eV for its relevance in solar energy harvesting applications) ( $f_{\max,\text{vis}}$ ); and the sum of oscillator strengths of all transitions in the visible window,  $f_{\text{sum,vis}}$ . These three features are also evaluated per  $n_{\pi}$  for the molecule, *i.e.*,  $f_{\max}/n_{\pi}$ ,  $f_{\max,\text{vis}}/n_{\pi}$  and  $f_{\text{sum,vis}}/n_{\pi}$ . We then consider the maximum absorption coefficient ( $\alpha_{\max}$ ) obtained using eqn (1) and (3); the maximum of the imaginary part of the dielectric function ( $\epsilon_{2,\max}$ );<sup>29</sup> and  $\epsilon_{d,\max}$ . Finally, we compute the spectral overlap between the OD ( $d\alpha(E)$ , where  $d$  is set to a typical film thickness value of 100 nm and  $\alpha(E)$  derives from the Gaussian-broadened spectrum of  $f$  in the visible spectral range taking a standard deviation of 0.1 eV) and the AM1.5G solar photon flux spectrum ( $\Phi_{\text{AM1.5G}}$ ), namely

$$f_{\text{overlap}} = \frac{\int_{1\text{eV}}^{4\text{eV}} \Phi_{\text{AM1.5G}}(E) d\alpha(E) dE}{\int_{1\text{eV}}^{4\text{eV}} \Phi_{\text{AM1.5G}}(E) dE}$$

These features, together with their corresponding histograms (Fig. S14, ESI<sup>†</sup>) in terms of Spearman's rank correlation coefficients ( $\rho$ ), are explained in more detail in Note S2 (ESI<sup>†</sup>). Molecular descriptors are calculated using up to four different open-source packages<sup>73–76</sup> (Note S2, ESI<sup>†</sup>) to generate a (curated) collection of 3239 entries (including 40 electronic descriptors derived from the TDDFT calculations, namely the energy of the molecular orbitals ranging from HOMO–19 to LUMO+19). Then, we scan for statistical correlations between those descriptors and all target features introduced above, from which we consider as highly correlated descriptors those showing  $\rho \geq 0.7$  as threshold. However, since some descriptors are calculated in groups or families where weighting factors are varied among atomic masses, van der Waals volumes, electronegativities, ionization potentials or polarizabilities, we usually encounter sets of multicollinear descriptors that show very similar trends with respect to the target feature. Accordingly, to drop redundant (collinear) descriptors we classify them into clusters to select the most representative candidate of each bundle (*i.e.*, cluster). This serves us to simplify the identification of characteristic and well-correlated descriptors families. The clustering algorithm applied to analyse multicollinear descriptors based on  $\rho$  and  $r$  values is further described in Note S3 (ESI<sup>†</sup>).

After running the clusterization of descriptors on all target features, we identify strong correlations with molecular descriptors for  $f_{\max}$ ,  $f_{\text{sum,vis}}$  and  $\epsilon_{d,\max}$  (*i.e.*, implicitly  $f_{\max,\text{vis}}$ ). For the remaining target variables ( $f_{\text{overlap}}$ ,  $\alpha_{\max}$ ,  $\epsilon_{2,\max}$ ,  $f_{\max}/n_{\pi}$ ,  $f_{\max,\text{vis}}/n_{\pi}$  and  $f_{\text{sum,vis}}/n_{\pi}$ ), we do not identify molecular descriptors with  $\rho$  above the threshold value (0.7) and they are generally below 0.6 units, see Fig. S14 (ESI<sup>†</sup>). The lack of correlation for  $f_{\text{overlap}}$  could be justified by the existence of a gas-to-solid shift in the corresponding absorption spectrum, which prevents proper



matching of the Gaussian-broadened absorption features with the solar photon flux. Regarding  $\alpha_{\max}$  and  $\varepsilon_{2,\max}$ , the estimation of these values from TDDFT calculations requires taking generalized assumptions on several materials properties (such as density or refractive index) that might be enough to disturb the underlying trends in our heterogeneous material database. For the quantities normalised by the number of pi electrons, *i.e.*  $f_{\max}/n_{\pi}$ ,  $f_{\max,\text{vis}}/n_{\pi}$  and  $f_{\text{sum,vis}}/n_{\pi}$ , the weak correlation is expected since normalization tends to deviate from linear correlations depending on the straightness of the molecule.<sup>29</sup> Due to the strong correlation between size of the molecule and oscillator strength as discussed below based on C2SP2, the normalised quantity is believed to be a secondary factor, therefore not clear correlations are observed. In the successful correlation cases (*i.e.*  $f_{\max}$ ,  $f_{\text{sum,vis}}$  and  $\varepsilon_{d,\max}$ ) and with the given thresholds of 0.7 units for  $\rho$  and  $r$ , we identify a single feature cluster lead by the  $\lambda_{1,p}$  descriptor in the case of  $f_{\max}$  and  $\varepsilon_{d,\max}$  (Fig. 2a). For  $f_{\text{sum,vis}}$ , a threshold  $\rho$  of 0.68 reveals C2SP2 as a rather descriptive molecular feature (Fig. 2b). Interestingly, C2SP2 is also found in the main cluster represented by  $\lambda_{1,p}$  in  $f_{\max}$  and  $\varepsilon_{d,\max}$ , and we could not identify any strong correlations between the absorption strength (in any of its proposed metrics) and electronic descriptors (from HOMO–19 to LUMO+19 energy levels). Note that  $\varepsilon_{d,\max}$  values in excess of

$2.5 \times 10^5 \text{ M}^{-1} \text{ cm}^{-1}$  in Fig. 2a and b are mostly attributed to artificially straight conjugated oligomers with >10 monomers contained in our database, for which the straightness, hence high  $\varepsilon_{d,\max}$ , are unlikely to be maintained in the experimental solid state scenario. In fact, only the exemplary and asymmetric NFA known as BDTP-4F (inset of Fig. 2a)<sup>77,78</sup> surpasses that threshold with a record  $\varepsilon_{d,\max}$  in our NFA dataset ( $2.7 \times 10^5 \text{ M}^{-1} \text{ cm}^{-1}$ , and  $2.4 \times 10^5 \text{ M}^{-1} \text{ cm}^{-1}$  measured in  $\text{CHCl}_3$  solution).<sup>77</sup>

$\lambda_{1,p}$  is part of a bundle of three-dimensional molecular size and shape descriptors known as weighted holistic invariant molecular (WHIM) descriptors.<sup>79–81</sup> These can be interpreted as a generalized search for the principal axes with respect to a defined atomic property.<sup>82</sup> In this particular case,  $\lambda_{1,p}$  is obtained by performing a principal component analysis (PCA) on the centred atomic coordinates of the molecule using a covariance matrix ( $s_{jk}$ ) that is weighted by the atomic polarizabilities ( $p_i$ ):

$$s_{jk} = \frac{\sum_{i=1}^A p_i (q_{ij} - \bar{q}_j)(q_{ik} - \bar{q}_k)}{\sum_{i=1}^A p_i}, \quad (4)$$

where  $s_{jk}$  is the weighted covariance between the  $j$ th and  $k$ th atomic coordinates;  $A$  is the total number of atoms;  $p_i$  is the

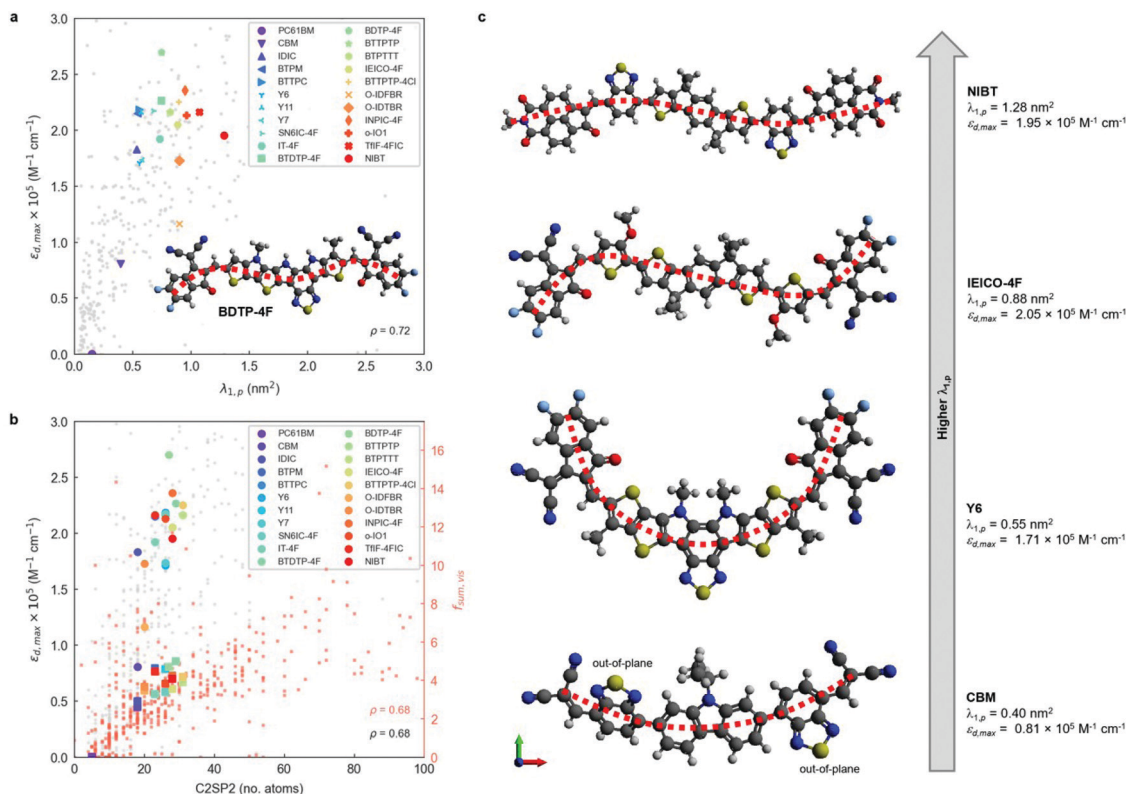


Fig. 2 (a) Correlation between, as calculated from TDDFT, and  $\lambda_{1,p}$  as obtained in the database of 479 molecules. The DFT-optimized geometry of BDTP-4F is shown in the inset. (b) Correlation between  $\varepsilon_{d,\max}$  (and  $f_{\text{sum,vis}}$  in the secondary axis) and C2SP2 in that same database. (c) DFT-optimized geometries of archetypal NFAs ordered by increased values of  $\lambda_{1,p}$  from bottom to top (CBM < Y6 < IEICO-4F < NIBT). Dotted red lines tentatively indicate the overall curvature of the main conjugated backbone of the molecule.  $\lambda_{1,p}$  and C2SP2 describe the size of the molecule in the direction of maximal atomic polarizability, and the number of doubly bound carbon atoms ( $\text{sp}^2$  hybridized) bound to two other carbons (C2), respectively.



(tabulated) polarizability of the  $i$ th atom;  $q_{ij}$  and  $q_{ik}$  represent the  $j$ th and  $k$ th coordinate of the  $i$ th atom ( $j, k = x, y, z$ ), respectively; and  $\bar{q}$  is their average value.<sup>82</sup> After diagonalization of the polarizability-weighted covariance matrix, the first eigenvalue ( $\lambda_{1,p}$ ) quantifies the size of the molecule in the direction of maximal polarizability variance. Interestingly, the third eigenvalue ( $\lambda_{3,p}$ ) approaches zero in planar molecules as a result of absence of variance in the out-of-plane ( $z$ ) direction.<sup>82</sup> On the other hand, C2SP2, which is not in the WHIM group, accounts for the number of doubly bound carbon atoms ( $sp^2$  hybridized, SP2) bound to two other carbons (C2), thus constituting a two-dimensional descriptor of fast computation. The correlation between C2SP2 and absorption strength can be relatively easier to understand, as C2SP2 to some extent represents the size of the conjugated molecule. Enlarging the size of the molecule increases the total number of  $\pi$ -electrons, which controls the total oscillator strength following the Thomas–Reiche–Kuhn rule. For the molecules that are extended along one direction, such as linear oligomers, increasing the size should enhance the oscillator strength of the first transition,<sup>29</sup> *i.e.* the dominant one.

To further interpret these two magnitudes ( $\lambda_{1,p}$  and C2SP2) as the main correlated descriptors with  $\varepsilon_{d,max}$  and  $f_{sum,vis}$ , we inspect the DFT-optimized geometries of archetypal NFAs (Fig. 2c). The observed trend suggests that optical extinction monotonically increases with  $\lambda_{1,p}$  (Fig. 2a) in molecules having most of their polarizable atoms arranged along a main axis, *i.e.*, linear molecules. While CBM shows large torsion angles mainly affecting the 2,1,3-benzothiadiazole (BT) moieties (thus making the molecule non-planar and increasing  $\lambda_{3,p}$ , see Fig. S15, ESI<sup>†</sup>), Y6 shows a characteristic curved geometry that limits its  $\varepsilon_{d,max}$  despite showing improved planarity. The NFA with the highest  $\lambda_{1,p}$  (NIBT) shows both linearity and planarity, with most of the more polarizable atoms (mainly C and S) lying along the principal polarizable axis of the molecule. Thus, in terms of molecular geometry, the absorption strength of NFAs could be further enhanced by distributing most of the atomic polarizability along a main axis while keeping good planarity and minimizing curvature. However,  $\lambda_{1,p}$  is not the sole molecular descriptor governing absorption strength, as BDTF-4F shows *ca.* 40% lower  $\lambda_{1,p}$  (0.75 nm<sup>2</sup>) yet *ca.* 40% higher  $\varepsilon_{d,max}$  than NIBT (Fig. 2a), which suggests that the molecular symmetry of NFAs could be another important factor affecting  $\varepsilon_{d,max}$ . Our preliminary investigations on this issue indicate that molecular asymmetry, as quantified by the WHIM symmetry index  $G_u$ , might drive absorption strength higher (Fig. S16a, ESI<sup>†</sup>), yet we require a larger NFA database including more asymmetric molecules to further explore such an observation. Also, we acknowledge that this observation might be biased by the systematic omission of side chains in the TDDFT calculations. By comparing  $\lambda_{1,p}$  in a selection of small molecule acceptors geometrically optimized with and without side chains (Fig. S17a, ESI<sup>†</sup>), we observe that in most cases the addition of side chains either decreases  $\lambda_{1,p}$  slightly or keeps it invariant. Still, the positive correlation of  $\lambda_{1,p}$  with respect to  $\varepsilon_{d,max}$  is maintained (Fig. S17b, ESI<sup>†</sup>). Furthermore, the presence of

naphthalene imide derivatives in the molecular structure of NIBT could be hindering further increase of the absorption strength with  $\lambda_{1,p}$ , as suggested by our statistical analysis of frequent moieties in the selection of good light harvesters (presented in the next section). On the other hand, an increase of  $n_\pi$  in the molecule in the form of closed-ring conjugated moieties will systematically increase C2SP2 and accordingly  $f_{sum,vis}$ . These findings support the previously known design rules in terms of molecular linearity and  $\pi$ -conjugation enabling large oscillator strength in organic small molecules and polymers, and are consistent with a recent study on chromophores.<sup>30</sup> In particular, trans-conjugated polymer stereoisomers are known to possess higher optical extinction due to their increased straightness and persistence length,<sup>29</sup> which agrees with our observations on exemplary curved (Y6) and more linear (NIBT) NFAs.

The energy of the first optical transition ( $E_1$ ) is also of practical importance in light harvesters such as NFAs as the lower energy part of the solar spectrum, down to  $\sim 1$  eV, contains a higher photon flux density. Our results show the number of heteroatoms in the molecule as the most correlated feature with ( $\rho = -0.72$ , Fig. S18a, ESI<sup>†</sup>) while forming a single feature cluster, yet neither  $\lambda_{1,p}$  nor C2SP2 show strong correlations with  $E_1$ . This fact prevents the introduction of molecular design rules targeted at  $E_1$  using  $\lambda_{1,p}$  or C2SP2. However, we acknowledge a negative correlation between  $E_1$  and  $f_{osc,max}$  among common NFAs that suggests further room for absorption strength increase as  $E_1$  is reduced (Fig. S19, ESI<sup>†</sup>).

**2.2.2. Chemical insights into highly absorbing molecules.** Beyond molecular descriptors, we investigate the relationship between the choice of moieties and absorption strength to provide further material design rules for highly absorbing conjugated small molecules. Our objective is to identify over-represented moieties in the subset of high-absorbing molecules (which we arbitrarily define as those having  $f_{osc,max} > 2.5$ , thus setting a population of size  $p$ ) with respect to the entire molecular dataset (population of size  $P$ ). Accordingly, we identify the molecular motifs present in the molecules by comparing their structures (as derived from SMILES notation) with those of a previously built database of moieties (also SMILES-based). This database of moieties was partly inherited from a previous work<sup>42</sup> and extended with further motifs present in our particular dataset (see Note S4 (ESI<sup>†</sup>) and the spreadsheet included as ESI<sup>†</sup>). Afterwards, we consider that a discrete hypergeometric distribution is adequate to model our molecular dataset and the fragments found therein<sup>42</sup> to calculate the corresponding  $Z$ -scores as  $Z = (k - \bar{k})/\sigma_k$ , where  $k$  is the number of high-absorbing molecules containing certain moiety; is its expected value, defined as  $pK/P$  where  $K$  corresponds to the number of molecules in the entire dataset containing that same moiety; and  $\sigma_k = \sqrt{pK(P-K)(P-p)/(P^2(P-1))}$  is the standard deviation of the hypergeometric distribution.  $Z$ -scores will indicate (in units of  $\sigma_k$ ) which moieties are overrepresented or underrepresented in the subset of high-performing molecules with respect to the expected values when looking at the entire dataset. Our results (Fig. 3) suggest that thieno[3,2-*b*]thiophene





(TT), thiophene (T), 2-(5,6-difluoro-3-oxo-2,3-dihydro-1*H*-inden-1-ylidene)malononitrile (2FIC), 2-(3-oxo-2,3-dihydro-1*H*-inden-1-ylidene)malononitrile (IC), indaceno[1,2-*b*:5,6-*b'*]dithiophene (IDT), 2-methylene malononitrile, cyanide, and aniline are particularly frequent in highly absorbing molecules. Interestingly, four of those molecular fragments (TT, T, 2FIC and IC) are contained in the chemical structure of the workhorse NFA Y6 (Fig. 2c). Contrarily, naphthalene imide derivatives, as typically encountered in n-type small molecules and conjugated polymers; 4*H*,8*H*-benzo[1,2-*c*:4,5-*c'*]dithiophene-4,8-dione and benzo[1,2-*b*:4,5-*b'*]dithiophene fragments are mostly underrepresented in the selection of high-performing light harvesters.

We further study the existing correlation between pairs of moieties to understand in which way the different molecular fragments should (or should not) be combined to retrieve highly-absorbing molecules. Our analysis starts by creating molecular subsets determined by the presence of a given moiety, which acts as source node (coloured in black) in the network graph shown in Fig. 3b. Within that subset, we identify the high-absorbing molecules ( $f_{\text{osc,max}} > 2.5$ ) and compute the Z-scores of their moieties (child nodes, coloured in grey in Fig. 3b) with respect to the molecules of the entire molecular subset. As per the network shown in Fig. 3b, the absolute Z-scores will determine the width of the edges connecting the nodes (moieties) and its sign the colour of the edge (green for positive Z-score [overrepresentation] and red for negative Z-score [underrepresentation]). Therefore, green and thick edges connect pairs of moieties that are more frequently found in high-absorbing molecules whereas thick and red edges indicate combinations of moieties that lead to less absorbing molecules. In this analysis, we set up 8 different source nodes corresponding to the most overrepresented moieties observed in Fig. 3a. As a result, Fig. 3b can be interpreted as a catalogue of design rules relating pairs of moieties with high oscillator strength in  $\pi$ -conjugated small molecules.

### 2.3. Machine-learning modelling of the absorption strength

Besides providing useful chemical insights from a material design perspective, molecular descriptors can be exploited to feed regression models and draw predictions on certain target features, forming the so-called quantitative structure–property relationship (QSPR) and quantitative structure–activity relationship (QSAR) models.<sup>79,80,82,83</sup> In the present study, we train and test several ML models fed with molecular and electronic descriptors obtained from TDDFT calculations to predict the value of  $\epsilon_{\text{d,max}}$  in conjugated small molecules and oligomers. Finally, we propose exploiting such ML model (trained with TDDFT data) to predict  $\epsilon_{\text{d,max}}$  in molecules optimized using a semi-empirical quantum chemistry method, *i.e.* xTB.<sup>84</sup> This renders possible thanks to the geometrical similarity of the TDDFT and xTB ground state conformers, which lead to similar (geometrical) descriptors values; and the calibration of their corresponding energy levels, as per the required inputs of the ML model herein employed. Therefore, further molecular candidates beyond the pristine dataset could be geometrically optimized using solely xTB Hamiltonians and their absorption strength predicted using such ML model. This approach effectively bypasses the use of TDDFT calculations when screening the absorption strength of novel molecules, which results in less demanding computations and higher throughput. The present ML workflow will open the possibility to accelerate the screening of high-performing molecular candidates with low-to-moderate computational requirements (further discussed in Note S5, ESI†).

**2.3.1. Modelling  $\epsilon_{\text{d,max}}$  with random decision forests.** From the analysis of descriptors shown in Section 2.2.1, we identified two main feature clusters represented by  $\lambda_{1,p}$  and C2SP2. We tentatively consider these two descriptors as independent variables in baseline models (such as 1-nearest neighbour and linear regression) targeted to  $\epsilon_{\text{d,max}}$ . For the model training and

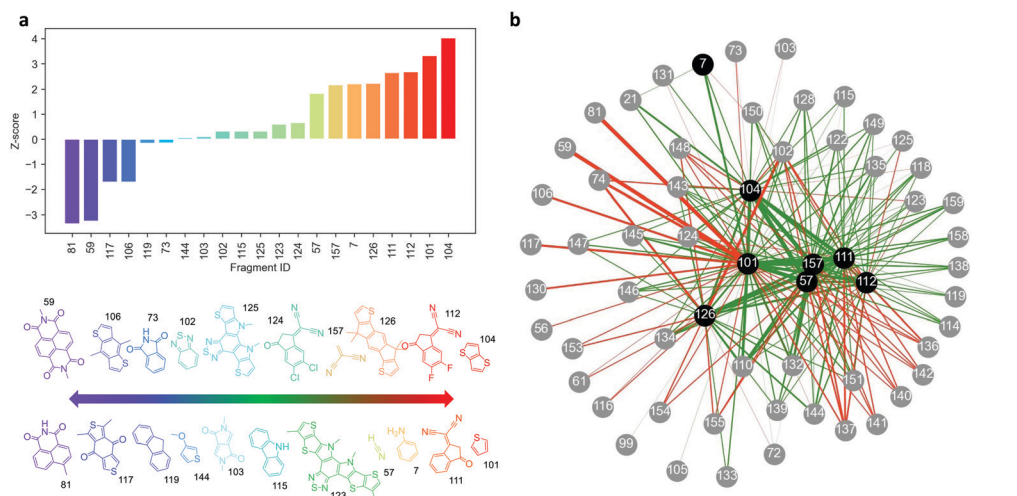


**Fig. 3** (a) Z-scores obtained from the discrete hypergeometric distribution of moieties in the highly-absorbing molecules ( $f_{\text{osc,max}} > 2.5$ ) with respect to the entire molecular dataset, for moieties activated at least 10 times. The corresponding structures of identified moieties are shown. (b) Network graph of Z-scores relating pairs of moieties. Source nodes are coloured in black whereas child nodes are coloured in grey. The colour of the edges corresponds to the sign of the Z-score (green for positive, red for negative). The width of the edges scales with the absolute value of the Z-score.





testing, we split our pristine dataset onto two subsets, namely the training set (gathering 70% of the data, randomly selected) and the testing set (gathering the remaining 30% of the data). Such baseline models are picked according to a recently introduced catalogue of good practices in the ML field,<sup>85</sup> to demonstrate the requirement of more advanced regressors (namely ML) in successful data modelling. The models are scored and quantitatively compared based on work-horse fitting metrics, such as their coefficient of determination ( $R^2$ ); their adjusted coefficient of determination ( $R_{\text{adj}}^2$ , which adds penalties as the number of parameters increases, see Note S2, ESI†); and their Pearson correlation coefficient ( $r$ ), as retrieved in the training (fitting) and test sets. The inherent mathematical simplicity of the baseline models results in poor fitting scorings (Fig. S20 and Table S1, ESI†) yet they suggest that feature selection procedures could end up in higher-performing models.

Accordingly, we deploy a state-of-the-art ML method, namely a RF, to aid in both aspects: feature selection and building of  $\epsilon_{\text{d,max}}$  models of higher accuracy. RFs constitute one of the simplest and most widely applied ML methods in molecular screening and data mining studies.<sup>30,43,46,86</sup> They are particularly appealing for their straightforward implementation through open-source Python libraries such as Scikit-Learn,<sup>87</sup> and also for their inherent robustness against overfitting and fast optimization. RFs are formed by an ensemble of decision trees (estimators) that are executed in parallel and independently from each other. Decision trees serve to classify data by starting from a single root node that is subsequently divided into child nodes, the latter being chosen randomly among the input features. At every node splitting step (*i.e.*, decision making), the algorithm selects the pathway that minimizes the mean square error (MSE). Eventually, when every tree reaches its maximum extension (which is set arbitrarily *via* model hyperparameters), the predictions of all trees are averaged (ensembled), hence constituting the final predicted value of the RF. At this stage, myriad cross-validation (CV) techniques exist to evaluate the quality of the model and help in the tuning of hyperparameters. CV methods can estimate the ML model performance, evaluate potential over- or underfitting, and quantify how accurate the model is on drawing predictions on unseen data. In this work, we adopt two common cross-validation schemes, namely a repeated holdout CV; and a leave-one-out cross-validation (LOOCV). On the one hand, in a repeated holdout CV the pristine dataset is randomly split onto two distinct subsets, namely the training (here gathering 70% of the data) and testing (the remaining fraction of data, *i.e.* 30%) subsets. The model is trained and tested on the respective subsets, and the corresponding statistical metrics ( $R^2$ ,  $r$ , MSE, *etc.*) annotated. Eventually, the process is repeated  $k$  times (10-fold in this work), and all metrics are averaged to evaluate the ML model performance (its CV score). On the other hand, in a LOOCV the holdout process is taken to the extreme as the testing subset consists of a single data point while the remaining data is used in the training step. The process runs recursively for all data, thus eventually all data points are used for training and testing in the LOOCV protocol. Yet being

computationally expensive, a LOOCV results in a more accurate estimate of model performance.

Table S1 (ESI†) includes the performance of an out-of-the-box RF model trained and cross-validated using 300 trees (estimators). Exemplary comparisons between the two previous baseline models (1-nearest neighbor and linear regression) and the out-of-the-box RF model are found in Fig. S20 (ESI†). The RF models indicate that scoring functions ( $R^2$ ,  $r$ ) well above 0.6–0.8 are feasible upon careful feature selection and further optimization of the RF regressor. Feature selection in RFs is usually performed by filtering variables based on their feature importance, which is a metric that accounts for how much a feature decreases the weighted variance in the node splitting steps of the decision trees. This property enables feature ranking to then apply myriad algorithms to filter out the least important variables as seen by the RF regressor. In this work, we perform a recursive feature elimination (RFE) procedure to the initial library of 3239 descriptors as described in Note S2 (ESI†). In a RFE protocol, a significant fraction of the initial population of features is dropped in successive training steps of the RF ensemble. Features are dropped based on their corresponding feature importance until reaching an arbitrarily low number of input variables, hence simplifying the original model. Our RFE analysis shows that a threshold average  $R^2$  of 0.70 is achieved using a 12-variable model ( $R^2 = 0.70 \pm 0.05$ ,  $r = 0.84 \pm 0.03$ ), which outperforms the RF model presented earlier while including a drastic reduction in the number of variables (from 3239 to 12). The sweet spot in model accuracy and number of degrees of freedom is found for the 10-variable model, which shows the maximum average  $R_{\text{adj}}^2$  ( $0.67 \pm 0.06$ ).

Notably, a threshold  $R^2$  of 0.60 is already achieved training a 3-parameter RF model ( $R^2 = 0.63 \pm 0.06$ ,  $R_{\text{adj}}^2 = 0.62 \pm 0.06$ ,  $r = 0.80 \pm 0.03$ ), which is particularly appealing given its simplicity. The resulting three-variable model includes one three-dimensional descriptor ( $\lambda_{1,v}$  or WHIM\_45, as computed by the RDKit library, Fig. 4a), one two-dimensional descriptor (CIC3, as computed by PaDEL software, Fig. 4b) and one electronic descriptor, in this case the energy level of the second molecular orbital below the frontier HOMO (HOMO–2, Fig. 4c).  $\lambda_{1,v}$  refers to the first eigenvalue of the covariance matrix weighted by the atomic van der Waals volumes; thus,  $\lambda_{1,v}$  is included in the multicollinear feature cluster represented by  $\lambda_{1,p}$  that we previously and statistically identified, showing nearly perfect correlation ( $r = 0.99$ ) with  $\lambda_{1,p}$ . Accordingly,  $\lambda_{1,v}$  can be exchanged by  $\lambda_{1,p}$  without loss of performance in the RF model. This finding confirms that the linearity of the molecule (either quantified in terms of polarizabilities or van der Waals volumes) plays a key role in determining its absorption strength in the form of  $\epsilon_{\text{d,max}}$ . On the other hand, CIC3 is a graph-based, third-order neighbourhood symmetry index<sup>82</sup> which lacks a straightforward interpretation due to its mathematical complexity. We observe, however, that it linearly scales as  $\log_2 A$ , with  $A$  being the total number of vertices (atoms) in the graph (molecule)<sup>82</sup> thus likely reflecting the size of  $\pi$ -conjugation as per the characteristics of our dataset. The interpretation of HOMO–2 as an important descriptor is more challenging, and



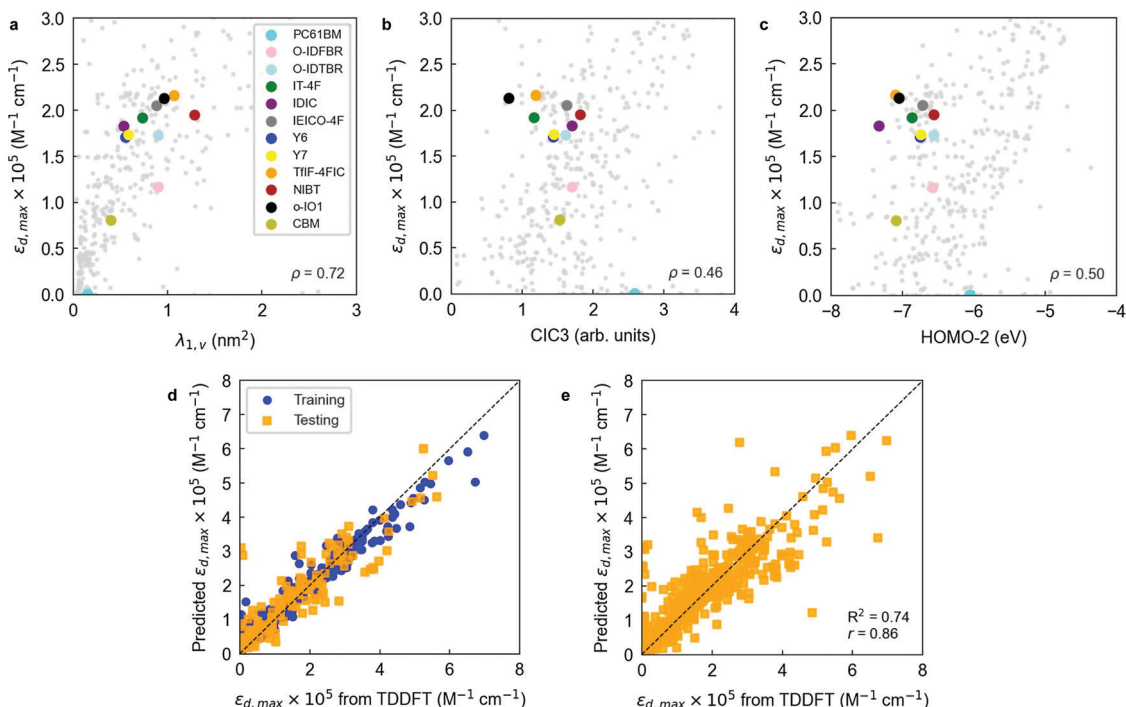


**Fig. 4** Correlation plots for  $\epsilon_{d,max}$  and the three most important descriptors retrieved by the RF model: (a)  $\lambda_{1,v}$ ; (b) CIC3; and (c) HOMO-2. (d) Holdout cross-validation run of a RF ensemble to predict  $\epsilon_{d,max}$ . 70% of the data is randomly selected for training and the remaining fraction is used for testing; the process is repeated 10 times and the statistical metrics averaged. The RF model is trained with three molecular descriptors ( $\lambda_{1,v}$ ; CIC3; and HOMO-2) and a Morgan fingerprint vector of 64 bits. (e) Leave-one-out cross-validation (LOOCV) of that same RF model using the optimized hyperparameter of 1200 estimators.

it is not possible to substitute it by a different descriptor without a noticeable drop in the model performance (excepting HOMO-1, which shows  $r = 0.96$ ).

Interestingly, electronic descriptors (in particular) are required for the RF models to achieve their highest potential and scoring despite we have not observed strong correlations in our earlier statistical analysis. To probe it, we have performed the same RFE protocol yet skipping the set of electronic descriptors among the input features. Our results show that the top performing RF models (selecting 29 variables and getting  $R^2 = 0.58 \pm 0.06$ ,  $R_{adj}^2 = 0.48 \pm 0.07$ ,  $r = 0.78 \pm 0.04$ ; or selecting 9 variables to obtain  $R_{adj}^2 = 0.52 \pm 0.06$ , see Fig. S13, ESI<sup>†</sup>) are yet behind the scorings recorded when the electronic descriptors are included in the list of features. Note that the performance without electronic descriptors is lower than the 3-parameter model that includes HOMO-2 as descriptor, highlighting its positive effect on the performance of the RF regressor.

Molecular fingerprints have also been extensively exploited as input vectorial descriptors in statistical and ML models focused on feature prediction.<sup>42,88–90</sup> Molecular fingerprints are usually represented as bit activation vectors of arbitrary length and degree of complexity, representing the absence or presence of certain molecular (bonding) pattern, moiety, functional group, or atom. In this work, we exploit the RDKit library to generate moiety fingerprints, MACCS keys, Morgan fingerprints, path-based or topological fingerprints, E-state

fingerprints, and Coulomb vectors. These fingerprints are quickly computed and serve to complement and improve the learning process of the ML models employed herein.

To better analyse the influence of the different fingerprint vectors in improving the RF scoring, we trained and cross-validated the 3-parameter RF model previously found in combination with all fingerprint vectors generated. The results shown in Table S2 (ESI<sup>†</sup>) indicate that by adding a Morgan fingerprint vector of 64 bits to the initial set of input features the model performance can be substantially improved:  $R^2$  increases by 10% (relative), and  $r$  by another (relative) 5% (see Fig. 4d). Therefore, Morgan fingerprints are particularly suitable to fine-tune the training and prediction accuracy of  $\epsilon_{d,max}$  in RF models although lacking of a straightforward physical interpretation. Additional refinement of the RF hyperparameters results in further improved models. We performed this optimization through a randomized search (in 350 iterations) of the hyperparameters controlling the number of estimators in the RF, the minimum number of samples per leaf node and the minimum number of samples required to split an internal node, which constitute the main adjustable hyperparameters of the RF algorithm. These results are shown in Table S3 (ESI<sup>†</sup>), together with the scoring obtained in a rigorous LOOCV of the optimized RF model (Fig. 4e). As an alternative ensemble of decision trees, we have also tested and optimized an Extra Trees (ET) regressor in Scikit-Learn. Its performance is, however, very close to that attained in the workhorse RF regressor (Table S3 and Fig. S21, ESI<sup>†</sup>).



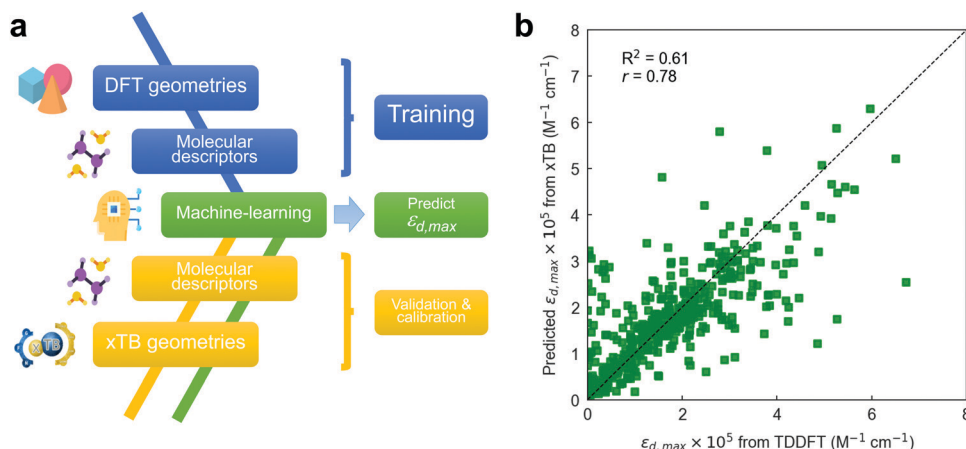


Fig. 5 (a) ML workflow used in this work to draw  $\epsilon_{d,max}$  predictions. A RF model is trained on TDDFT data and interpolated (validated) on xTB geometries, including also their corresponding molecular descriptors. To improve the accuracy of the model, energy levels obtained using the GFN2-xTB Hamiltonian require calibration with TDDFT values (Fig. S23, ESI<sup>†</sup>). (b) Leave-one-out interpolation of the resulting RF model using three input molecular descriptors (including calibrated energy levels) and a 64-bit Morgan fingerprint vector.

**2.3.2. Bypassing TDDFT calculations through machine-learning and extended tight-binding.** xTB Hamiltonians have recently emerged as semi-empirical and low computational cost quantum chemistry methods.<sup>84</sup> These have a remarkable potential in molecular screening when implemented in multi-level workflows where xTB is exploited first to identify plausible candidates using a minimal fraction of computational resources, to then leave room for higher-level DFT methods in selected candidates.<sup>84</sup> In this work, we propose exploiting a ML model trained with DFT data to predict  $\epsilon_{d,max}$  in molecular geometries optimized using xTB (Fig. 5a). This is expected to enable faster molecular screening and geometrical optimization steps, as both being entirely run using xTB Hamiltonians; followed by absorption strength ( $\epsilon_{d,max}$ ) prediction in a TDDFT-trained RF model. Notably, our estimations show that the geometrical optimization step using GFN2-xTB is *ca.* 3000 times faster than using DFT with a hybrid functional (B3LYP/6-311+G(d,p)), as discussed in Note S5 and Table S4 (ESI<sup>†</sup>).

Nevertheless, the dissimilarity between xTB- and DFT-optimized molecular geometries might have a direct impact on the value of the (three-dimensional) molecular descriptors, and hence on the final accuracy of the interpolated ML model if some of those are included. Accordingly, we have first quantitatively compared both sets of molecular (non-electronic) descriptors by computing  $r$  in all of them and found that the median of their distributions is very close to unity in all cases (Fig. S22, ESI<sup>†</sup>). Based on this finding, we proceed by training the RF model with TDDFT-derived descriptors and exploring how well the model interpolates when fed with xTB-derived descriptors. Fig. S23a (ESI<sup>†</sup>) shows a leave-one-out interpolation of a RF model trained using TDDFT data and interpolated on GFN2-xTB-optimized molecules, descriptors and energy levels.<sup>84,91,92</sup> In this kind of model validation, all TDDFT data is used in the training step excepting that for a single molecule, for which we retrieve its corresponding xTB-optimized geometry and descriptors as the sole interpolation (testing) dataset; this procedure is subsequently repeated for all molecules. Thus, the model performance is assessed by comparing the actual

TDDFT-derived  $\epsilon_{d,max}$  of the molecules ( $x$ -axis in Fig. 5b) with that predicted by a RF model trained with TDDFT data and interpolated using xTB-derived descriptors ( $y$ -axis in Fig. 5b). This is useful to evaluate whether such RF model fed with TDDFT data could be exploited to predict  $\epsilon_{d,max}$  in unseen molecules that are geometrically optimized through xTB Hamiltonians.

Our first model takes as inputs the three molecular descriptors found previously to be the most important features in the RF model together with their corresponding (64-bit) Morgan fingerprints. The scoring of the LOOCV in this preliminary model ( $R^2 = 0.53$ ,  $r = 0.74$ ) is limited due to the existence of a mismatch between the absolute energy levels retrieved by either DFT (B3LYP) or GFN2-xTB methods (Fig. S23b, ESI<sup>†</sup>). Thus, the RF model trained on TDDFT data needs proper calibration of the energy levels obtained through GFN2-xTB, which we perform using either a linear regression, a support vector regressor (SVR) or an additional RF model (Fig. S23c, ESI<sup>†</sup>). By applying such calibration on the HOMO-2 energy levels, we obtain the champion RF model ( $R^2 = 0.61$ ,  $r = 0.78$ ) shown in Fig. 5b using three molecular descriptors and a 64-bit Morgan fingerprint vector. Hence, Fig. 5b shows that molecular databases of xTB-optimized geometries could be exploited in combination with TDDFT-trained ML models to predict the absorption strength ( $\epsilon_{d,max}$ ) at significantly lower computational cost and with reasonable accuracy. The statistical analysis and ML modelling framework introduced here is thus expected to show large potential in the high-throughput screening of highly absorbing molecular candidates in combination with generative models (autoencoders and neural networks) as part of future work in the group.

### 3. Conclusion

We have demonstrated that TDDFT calculations agree reasonably well with the experimental maximum molar extinction coefficient ( $\epsilon_{d,max}$ ) in solution state by exploiting a database of TDDFT-optimized small molecular acceptors (NFAs) and donor





oligomers collected over the years. This finding supports further analysis of the molecular dataset to identify structure–absorption relationships by means of statistical and machine-learning (ML) methods. Through the exploration of molecular descriptors, we identify two features that are strongly correlated with  $\epsilon_{d,\max}$ , namely the linearity and planarity of the molecule in the direction of maximum atomic polarizability variance; and the number of  $sp^2$ -hybridized carbon atoms bonded to two other carbons included in the molecule. These further suggest design rules that highly absorbing organic  $\pi$ -conjugated molecules (such as NFAs) should follow, namely a fully conjugated, planar and linear molecular backbone with more polarisable heteroatoms. We further identify that moieties such as thieno-[3,2-*b*]thiophene (TT), thiophene (T), 2-(5,6-difluoro-3-oxo-2,3-dihydro-1*H*-inden-1-ylidene)malononitrile (2FIC), 2-(3-oxo-2,3-dihydro-1*H*-inden-1-ylidene)malononitrile (IC) and indaceno-[1,2-*b*:5,6-*b'*]dithiophene (IDT) appear more frequently in molecules with the highest absorption strength. Finally, we demonstrate the feasibility of random decision forests (RFs) trained with a few (3) molecular descriptors and 64-bit Morgan fingerprint vectors to predict in molecular geometries optimized by a computationally less demanding method such as extended tight-binding ( $\times$ TB). This approach shows the ability to bypass thorough TDDFT calculations, thus facilitating high-throughput screening of absorption strength in organic  $\pi$ -conjugated molecules in combination with generative molecular models.

## 4. Outlook

This work was motivated by the search for molecular design rules to enable higher PCE in organic solar cells. Although maximizing light absorption for a given optical band gap is a key requirement to enable record PCE, many additional physical processes contribute to photovoltaic performance but are not considered directly in the present work, namely, exciton diffusion, charge transfer, charge separation, charge transport and charge recombination. To date, there is no holistic modelling framework nor are there sufficient data to relate these multiple processes to device performance *via* chemical structure. However, developments in AI and ML methods are likely to advance the status of models for multiple property–device performance relationships in the coming years.

Nevertheless, understanding how light harvesting alone can be maximized by smart molecular design is significant for improving several different aspects of OPV performance. Light absorption is the primary step towards charge generation and is therefore strongly related to the macroscopic short-circuit current density of the device. According to the reciprocity relation between absorption and emission,<sup>20</sup> high absorption should in principle lead to strong emission, therefore reducing the nonradiative energy losses, and benefitting the open-circuit voltage. In addition, high absorption allows the fabrication of thin devices, therefore facilitating charge extraction and enhancing fill factor.<sup>93</sup> Moreover, based on the causality principle, high absorption strength would lead to higher refractive index,

which takes the first interference maximum of electric field to lower thicknesses, resulting in large light harvesting potential in thinner devices. Therefore, designing highly absorbing organic  $\pi$ -conjugated molecules has the potential to enhance different aspects relating to the performance of OPVs in conjunction with the proposed predictive ML model.

A separate aspect for future work is the impact of solid-state molecular interactions on light absorption. This paper concerns the optical absorption of isolated molecules while applications normally require thin films of molecules. Although intermolecular interactions can strongly impact the strength as well as the spectrum of thin film absorption,<sup>94</sup> this has been neglected in the present study due to the lack of a suitable database of computations and the lack of solid state packing information. In the future, ML approaches could be used to better understand and predict how solid state interactions affect optical absorption, and thereby improve molecular design rules. Such advances may be enabled by the growing capability in computational structure prediction as well as improved understanding of the impact of intermolecular interactions on excited state properties.

## 5. Experimental and theoretical methods

Excited state calculation database and experimental  $\epsilon_{d,\max}$  database: TDDFT results in this study are based on the functional B3LYP and were performed by present and past group members in Prof. Jenny Nelson's group at Imperial College London, making up more than 3500 entries (corresponding to 479 unique molecules). The majority of experimental solid state thin film  $\epsilon_{d,\max}$  values for NFAs shown in Fig. 1a–c were measured using variable-angle spectroscopic ellipsometry (VASE) for the present study. Neat films were deposited from solution by either spin- or blade-coating on glass substrates at distinct thicknesses (typically ranging from 30 to 150 nm). Ellipsometry data were acquired at three to five angles of incidence ( $55^\circ$ – $75^\circ$ ) using a Sopralab GES-5E rotating polarizer spectroscopic ellipsometer (SEMILAB) coupled to a charge-coupled device (CCD) detector. Experimental solution  $\epsilon_{d,\max}$  were mostly collected from literature with a majority of data taken from ref. 95, and Y5, Y6, and Y7 measured using UV-visible spectroscopy. The complete database and sources are presented in the ESI.†

Theoretical description of molar extinction coefficient ( $\epsilon_d$ ): to calculate the molar extinction coefficient  $\epsilon_d$ , let us start with defining the absorption coefficient  $\alpha$  in a quantum picture (we stay with SI units for the moment). The absorption coefficient for transition from state 1 to state 2 can be defined as<sup>19,96</sup>

$$\frac{dI}{dx} = -\alpha I, \quad (5)$$

where  $I$  is light intensity, determined by the energy density of an electromagnetic wave *via*

$$I = \frac{1}{2}nc\epsilon_0|E_0|^2, \quad (6)$$



where  $n$  is the refractive index,  $\epsilon_0$  vacuum permittivity,  $c$  the speed of light, and  $E_0$  the amplitude of the electric field. For an electromagnetic wave, the rate of intensity attenuation  $\frac{dI}{dx}$  is equal to the rate of loss of energy density from the field  $-\frac{dU}{dt}$ , and the latter is the product of transition rate  $\Gamma_{12}$  and transition energy  $\hbar\omega_{12}$ , and we have

$$\frac{dI}{dx} = -N\Gamma_{12}\hbar\omega_{12}, \quad (7)$$

where  $N$  is the volume density of molecules and  $\hbar$  the reduced Planck constant. Substituting for  $\frac{dI}{dx}$  and  $I$  in the definition of  $\alpha_{12}$  we get

$$\alpha_{12} = \frac{2N\hbar\omega_{12}\Gamma_{12}}{nc\epsilon_0|E_0|^2} \quad (8)$$

The transition rate  $\Gamma_{12}$  can be defined by Fermi's Golden Rule and the perturbing Hamiltonian given by  $H = d_{12}E_0$  using dipole approximation, where  $d_{12}$  is the transition dipole moment of the transition. Considering randomly oriented transition dipoles relative to the direction of the exciting electromagnetic field, we have

$$\Gamma_{12} = \frac{2\pi}{3\hbar}d_{12}^2|E_0|^2\delta(\hbar\omega - E_2 + E_1) \quad (9)$$

Using  $E_2 - E_1 = \hbar\omega_{12}$ , we get

$$\alpha_{12} = \frac{4\pi N\omega_{12}}{3nc\epsilon_0\hbar}d_{12}^2\delta(\omega - \omega_{12}) \quad (10)$$

From an arbitrary transition from state  $i$  to state  $j$ , we can express above equation using oscillator strength of the transition ( $f_{ij}$ ):

$$\alpha_{ij} = \frac{2\pi Ne^2}{3\epsilon_0 m_0 n c} f_{ij} \delta(\omega - \omega_{ij}), \quad (11)$$

where  $e$  is the elementary charge, and  $f_{ij} = \frac{2m_0\omega_{12}}{e^2\hbar}d_{ij}^2$ . Integrating over all transitions, we have

$$\alpha(\omega) = \frac{2\pi Ne^2}{3\epsilon_0 m_0 n c} \sum_{ij} f_{ij} \delta(\omega - \omega_{ij}) \quad (12)$$

To correlate the absorption coefficient ( $\alpha$ ) with the molar extinction coefficient ( $\epsilon_d$ ), we need the definition of optical density (OD) and optical depth ( $\alpha d$ ). Light is attenuated by passing through a depth  $d$  of material such that

$$I(d) = I_0 e^{-\alpha d} = I_0 10^{-\text{OD}} \quad (13)$$

And optical density, or called sometimes absorbance is defined as.

$$\text{OD} = \rho \epsilon_d d, \quad (14)$$

where  $\rho$  is concentration in molar (M or mol L<sup>-1</sup>), and  $d$  is sample length in cm. Consequently, we have

$$\epsilon_d = \frac{\log_{10}(e)}{\rho} \alpha_{\text{cm}} = \frac{\alpha_{\text{cm}}}{2.303\rho}, \quad (15)$$

noting that we now write the absorption coefficient per cm to distinguish from the expression for  $\alpha$  above, which we did assuming SI units, hence  $\alpha_{\text{cm}} = \frac{\alpha}{100}$ .  $\rho$  is moles of molecules per dm<sup>3</sup>. We now have

$$\epsilon_d(\omega) = 10 \log_{10}(e) N_A \frac{2\pi e^2}{3\epsilon_0 m_0 n c} \sum_{ij} f_{ij} \delta(\omega - \omega_{ij}) \quad (16)$$

Let us recast this in terms of photon energy  $E$  in eV, *i.e.*  $E = \frac{\hbar\omega}{e}$ , rather than angular frequency, so it is easier to consider the magnitude, and finally we have  $\epsilon_d$  in the unit of M<sup>-1</sup> cm<sup>-1</sup>.

$$\epsilon_d(E) = 10 \log_{10}(e) N_A \frac{2\pi e\hbar}{3\epsilon_0 m_0 n c} \sum_{ij} f_{ij} \delta(E - E_{ij}) \quad (17)$$

This allows us to compute the theoretical  $\epsilon_d$  using the calculated oscillator strength at different transitions. And the common method to calculate the oscillator strength is time-dependent-density-functional-theory (aka TDDFT).

Converting complex refractive index from solid state ellipsometry measurements to  $\epsilon_d$ : using ellipsometry measurements from film (solid state), we can extract the complex refractive index,  $\eta$

$$\eta = n + i\kappa \quad (18)$$

where  $n$  is the refractive index, and  $\kappa$  the extinction coefficient. The absorption coefficient ( $\alpha_{\text{cm}}$ ) is then determined by

$$\alpha_{\text{cm}} = \frac{4\pi\kappa}{\lambda_{\text{cm}}} \quad (19)$$

where  $\lambda_{\text{cm}}$  is the wavelength in centimetre. Using eqn (15), and the relationship between molar concentration  $\rho$  and mass concentration  $\rho_M$ , *i.e.*,  $\rho = \frac{\rho_M}{M_w}$ , we have

$$\epsilon_d = \log_{10}(e) \alpha_{\text{cm}} \frac{M_w}{\rho_M} = \log_{10}(e) \frac{4\pi\kappa M_w}{\lambda_{\text{cm}} \rho_M} \quad (20)$$

where  $M_w$  is the molecular weight, g mol<sup>-1</sup>, and  $\rho_M$  has the unit of g L<sup>-1</sup>, and is typically assumed to be 1000 g L<sup>-1</sup>.

## Author contributions

J. Y. and X. R.-M. contributed equally to this work and drafted the paper. J. Y. performed DFT and TDDFT calculations, absorption strength analysis, and data collection. X. R.-M. performed the statistical analysis and machine-learning study. D. P., H. D., D. B., M. A., A. V., S. F., A. A. S., and X. H. shared their DFT/TDDFT calculation results. F. E. prepared thin films of NFAs for VASE measurements. X. R.-M., V. B., and B. D. did VASE measurements. E. R. did UV-vis measurements of Y5, Y6, and Y7 in solution. G. Z. and H.-L. Y. provided Y5, Y6, and Y7. All authors gave critical review on this work. J. N. and M. C.-Q. supervised this work.

## Conflicts of interest

There are no conflicts to declare.



## Acknowledgements

J. N., J. Y., D. P., M. A., F. E., and E. R. thank the European Research Council for support under the European Union's Horizon 2020 research and innovation program (Grant Agreement No. 742708 and 648901). The authors at ICMAB acknowledge financial support from the Spanish Ministry of Science and Innovation through the Severo Ochoa Program for Centers of Excellence in R&D (No. CEX2019-000917-S), and project PGC2018-095411-B-I00. E. R. is grateful to the Fonds de Recherche du Quebec-Nature et technologies (FRQNT) for a postdoctoral fellowship and acknowledges financial support from the European Cooperation in Science and Technology. M. A. thanks the Engineering and Physical Sciences Research Council (EPSRC) for support *via* doctoral studentships. F. E. thanks the Engineering and Physical Sciences Research Council (EPSRC) for support *via* the Post-Doctoral Prize Fellowship. X. R.-M. acknowledges Prof. Olle Inganäs and the Knut and Alice Wallenberg Foundation for funding of his current postdoctoral position. H.-L. Yip thanks the support from Guangdong Major Project of Basic and Applied Basic Research (2019B030302007). The TOC figure and Fig. 5a in the manuscript include freely available resources from [Flaticon.com](http://Flaticon.com). J. Y. thank Xiaodan Ge for her support.

## References

- J. Nelson, *Mater. Today*, 2011, **14**, 462–470.
- G. Li, R. Zhu and Y. Yang, *Nat. Photonics*, 2012, **6**, 153–161.
- A. J. Heeger, *Adv. Mater.*, 2014, **26**, 10–28.
- M. Mainville and M. Leclerc, *ACS Energy Lett.*, 2020, **5**, 1186–1197.
- H. K.-H. Lee, J. Wu, J. Barbé, S. M. Jain, S. Wood, E. M. Speller, Z. Li, F. A. Castro, J. R. Durrant and W. C. Tsoi, *J. Mater. Chem. A*, 2018, **6**, 5618–5626.
- Y. Cui, Y. Wang, J. Bergqvist, H. Yao, Y. Xu, B. Gao, C. Yang, S. Zhang, O. Inganäs, F. Gao and J. Hou, *Nat. Energy*, 2019, **4**, 768–775.
- Y. Li, J. D. Lin, X. Che, Y. Qu, F. Liu, L. S. Liao and S. R. Forrest, *J. Am. Chem. Soc.*, 2017, **139**, 17114–17119.
- S. Difley and T. Van Voorhis, *J. Chem. Theory Comput.*, 2011, **7**, 594–601.
- C. J.-M. Emmott, J. A. Röhr, M. Campoy-Quiles, T. Kirchartz, A. Urbina, N. J. Ekins-Daukes and J. Nelson, *Energy Environ. Sci.*, 2015, **8**, 1317–1328.
- C. J.-M. Emmott, D. Moia, P. Sandwell, N. Ekins-Daukes, M. Hösel, L. Lukoschek, C. Amarasinghe, F. C. Krebs and J. Nelson, *Sol. Energy Mater. Sol. Cells*, 2016, **149**, 284–293.
- L. Zhu, M. Zhang, J. Xu, C. Li, J. Yan, G. Zhou, W. Zhong, T. Hao, J. Song, X. Xue, Z. Zhou, R. Zeng, H. Zhu, C.-C. Chen, R. C.-I. MacKenzie, Y. Zou, J. Nelson, Y. Zhang, Y. Sun and F. Liu, *Nat. Mater.*, 2022, 1–8, DOI: [10.1038/s41563-022-01244-y](https://doi.org/10.1038/s41563-022-01244-y).
- J. Zhao, Y. Li, G. Yang, K. Jiang, H. Lin, H. Ade, W. Ma and H. Yan, *Nat. Energy*, 2016, **1**, 15027.
- P. Cheng, G. Li, X. Zhan and Y. Yang, *Nat. Photonics*, 2018, **12**, 131–142.
- Y. Wang, J. Lee, X. Hou, C. Labanti, J. Yan, E. Mazzolini, A. Parhar, J. Nelson, J. Kim and Z. Li, *Adv. Energy Mater.*, 2021, **11**, 2003002.
- J. Hou, O. Inganäs, R. H. Friend and F. Gao, *Nat. Mater.*, 2018, **17**, 119–128.
- J. Yuan, Y. Zhang, L. Zhou, G. Zhang, H.-L. Yip, T.-K. Lau, X. Lu, C. Zhu, H. Peng, P. A. Johnson, M. Leclerc, Y. Cao, J. Ulanski, Y. Li and Y. Zou, *Joule*, 2019, **3**, 1140–1151.
- M. Kaltenbrunner, M. S. White, E. D. Glowacki, T. Sekitani, T. Someya, N. S. Sariciftci and S. Bauer, *Nat. Commun.*, 2012, **3**, 1–7.
- W. Yang, W. Wang, Y. Wang, R. Sun, J. Guo, H. Li, M. Shi, J. Guo, Y. Wu, T. Wang, G. Lu, C. J. Brabec, Y. Li and J. Min, *Joule*, 2021, **5**, 1209–1230.
- J. Nelson, *The Physics of Solar Cells*, Imperial College Press, 2003.
- U. Rau, *Phys. Rev. B*, 2007, **76**, 085303.
- M. Azzouzi, J. Yan, T. Kirchartz, K. Liu, J. Wang, H. Wu and J. Nelson, *Phys. Rev. X*, 2018, **8**, 031055.
- F. D. Eisner, M. Azzouzi, Z. Fei, X. Hou, T. D. Anthopoulos, T. J.-S. J.-S. Dennis, M. Heeney and J. Nelson, *J. Am. Chem. Soc.*, 2019, **141**, 6362–6374.
- J. Yan, E. Rezasoltani, M. Azzouzi, F. Eisner and J. Nelson, *Nat. Commun.*, 2021, **12**, 3642.
- A. Classen, C. L. Chochos, L. Lüer, V. G. Gregoriou, J. Wortmann, A. Osvet, K. Forberich, I. McCulloch, T. Heumüller and C. J. Brabec, *Nat. Energy*, 2020, **5**, 711–719.
- X.-K. Chen, D. Qian, Y. Wang, T. Kirchartz, W. Tress, H. Yao, J. Yuan, M. Hülsbeck, M. Zhang, Y. Zou, Y. Sun, Y. Li, J. Hou, O. Inganäs, V. Coropceanu, J.-L. Bredas and F. Gao, *Nat. Energy*, 2021, **6**, 799–806.
- J. Benduhn, K. Tvingstedt, F. Piersimoni, S. Ullbrich, Y. Fan, M. Tropiano, K. A.-A. McGarry, O. Zeika, M. K.-K. Riede, C. J.-J. Douglas, S. Barlow, S. R.-R. Marder, D. Neher, D. Spoltore and K. Vandewal, *Nat. Energy*, 2017, **2**, 17053.
- X.-K. Chen, V. Coropceanu, J.-L. Bredas and J.-L. Bredas, *Nat. Commun.*, 2018, **9**, 5295.
- D. Qian, Z. Zheng, H. Yao, W. Tress, T. R. Hopper, S. S. Chen, S. Li, J. Liu, S. S. Chen, J. Zhang, X.-K. K. Liu, B. Gao, L. Ouyang, Y. Jin, G. Pozina, I. A. Buyanova, W. M. Chen, O. Inganäs, V. Coropceanu, J.-L. L. Bredas, H. Yan, J. Hou, F. Zhang, A. A. Bakulin and F. Gao, *Nat. Mater.*, 2018, **17**, 703–709.
- M. S. Vezie, S. Few, I. Meager, G. Pieridou, B. Dörling, R. S. Ashraf, A. R. Goñi, H. Bronstein, I. McCulloch, S. C. Hayes, M. Campoy-Quiles and J. Nelson, *Nat. Mater.*, 2016, **15**, 746–753.
- B. Kang, C. Seok and J. Lee, *J. Chem. Inf. Model.*, 2020, **60**, 5984–5994.
- S. Few, J. M. Frost, J. Kirkpatrick and J. Nelson, *J. Phys. Chem. C*, 2014, **118**, 8253–8261.
- Y. Yi, V. Coropceanu and J.-L. Bredas, *J. Mater. Chem.*, 2011, **21**, 1479.
- T. Liu and A. Troisi, *J. Phys. Chem. C*, 2011, **115**, 2406–2415.
- J. C. Slater, *Phys. Rev.*, 1951, **81**, 385.





- 35 B. L. Hammond, W. A. Lester and P. J. Reynolds, *Monte Carlo Methods in Ab Initio Quantum Chemistry*, World Scientific, 1994, vol. 1.
- 36 R. A. Friesner, *Proc. Natl. Acad. Sci. U. S. A.*, 2005, **102**, 6648–6653.
- 37 Y. Shao, L. F. Molnar, Y. Jung, J. Kussmann, C. Ochsenfeld, S. T. Brown, A. T. B. Gilbert, L. V. Slipchenko, S. V. Levchenko, D. P. O'Neill, R. A. DiStasio Jr, R. C. Lochan, T. Wang, G. J. O. Beran, N. A. Besley, J. M. Herbert, C. Yeh Lin, T. Van Voorhis, S. Hung Chien, A. Sodt, R. P. Steele, V. A. Rassolov, P. E. Maslen, P. P. Korambath, R. D. Adamson, B. Austin, J. Baker, E. F. C. Byrd, H. Dachsel, R. J. Doerksen, A. Dreuw, B. D. Dunietz, A. D. Dutoi, T. R. Furlani, S. R. Gwaltney, A. Heyden, S. Hirata, C.-P. Hsu, G. Kedziora, R. Z. Khallilulin, P. Klunzinger, A. M. Lee, M. S. Lee, W. Liang, I. Lotan, N. Nair, B. Peters, E. I. Proynov, P. A. Pieniazek, Y. Min Rhee, J. Ritchie, E. Rosta, C. David Sherrill, A. C. Simmonett, J. E. Subotnik, H. Lee Woodcock III, W. Zhang, A. T. Bell, A. K. Chakraborty, D. M. Chipman, F. J. Keil, A. Warshel, W. J. Hehre, H. F. Schaefer III, J. Kong, A. I. Krylov, P. M. W. Gill and M. Head-Gordon, *Phys. Chem. Chem. Phys.*, 2006, **8**, 3172–3191.
- 38 P. Raccuglia, K. C. Elbert, P. D.-F. Adler, C. Falk, M. B. Wenny, A. Mollo, M. Zeller, S. A. Friedler, J. Schrier and A. J. Norquist, *Nature*, 2016, **533**, 73–76.
- 39 K. T. Butler, D. W. Davies, H. Cartwright, O. Isayev and A. Walsh, *Nature*, 2018, **559**, 547–555.
- 40 J. Westermayr and P. Marquetand, *Chem. Rev.*, 2021, **121**, 9873–9926.
- 41 F. Häse, L. M. Roch, P. Friederich and A. Aspuru-Guzik, *Nat. Commun.*, 2020, **11**, 1–11.
- 42 S. A. Lopez, B. Sanchez-Lengeling, J. de Goes Soares and A. Aspuru-Guzik, *Joule*, 2017, **1**, 857–870.
- 43 H. Sahu, W. Rao, A. Troisi and H. Ma, *Adv. Energy Mater.*, 2018, **8**, 1–9.
- 44 W. K. Tatum, D. Torrejon, A. B. Resing, J. W. Onorato and C. K. Luscombe, *Comput. Mater. Sci.*, 2021, **197**, 110599.
- 45 N. Majeed, M. Saladina, M. Krompiec, S. Greedy, C. Deibel and R. C.-I. MacKenzie, *Adv. Funct. Mater.*, 2019, 1907259.
- 46 X. Rodríguez-Martínez, E. Pascual-San-José, Z. Fei, M. Heeney, R. Guimerà and M. Campoy-Quiles, *Energy Environ. Sci.*, 2021, **14**, 986–994.
- 47 X. Rodríguez-Martínez, E. Pascual-San-José and M. Campoy-Quiles, *Energy Environ. Sci.*, 2021, **14**, 3301–3322.
- 48 K. Kranthiraja and A. Saeki, *Adv. Funct. Mater.*, 2021, **31**, 1–11.
- 49 E. O. Pyzer-Knapp, C. Suh, R. Gómez-Bombarelli, J. Aguilera-Iparraguirre and A. Aspuru-Guzik, *Annu. Rev. Mater. Res.*, 2015, **45**, 195–216.
- 50 J. Hachmann, R. Olivares-amaya, S. Atahan-evrenk, C. Amador-bedolla, R. S. Sanchez-carrera, A. Gold-parker, L. Vogt, A. M. Brockway and A. Aspuru-Guzik, *J. Phys. Chem. Lett.*, 2011, **2**, 2241–2251.
- 51 A. Mahmood and J.-L. Wang, *Energy Environ. Sci.*, 2021, **14**, 90–105.
- 52 P. Malhotra, S. Biswas, F.-C. Chen and G. D. Sharma, *Sol. Energy*, 2021, **228**, 175–186.
- 53 A. Kuzmich, D. Padula, H. Ma and A. Troisi, *Energy Environ. Sci.*, 2017, **10**, 395–401.
- 54 I. Y. Kanal, S. G. Owens, J. S. Bechtel and G. R. Hutchison, *J. Phys. Chem. Lett.*, 2013, **4**, 1613–1623.
- 55 L. Wilbraham, E. Berardo, L. Turcani, K. E. Jelfs and M. A. Zwijnenburg, *J. Chem. Inf. Model.*, 2018, **58**, 2450–2459.
- 56 E. O. Pyzer-Knapp, K. Li and A. Aspuru-Guzik, *Adv. Funct. Mater.*, 2015, **25**, 6495–6502.
- 57 J. Hachmann, R. Olivares-Amaya, A. Jinich, A. L. Appleton, M. A. Blood-Forsythe, L. R. Seress, C. Román-Salgado, K. Treppe, S. Atahan-Evrenk, S. Er, S. Shrestha, R. Mondal, A. Sokolov, Z. Bao and A. Aspuru-Guzik, *Energy Environ. Sci.*, 2014, **7**, 698–704.
- 58 N. Bérubé, V. Gosselin, J. Gaudreau and M. Côté, *J. Phys. Chem. C*, 2013, **117**, 7964–7972.
- 59 S. Nagasawa, E. Al-Naamani and A. Saeki, *J. Phys. Chem. Lett.*, 2018, **9**, 2639–2646.
- 60 Y. Huang, J. Zhang, E. S. Jiang, Y. Oya, A. Saeki, G. Kikugawa, T. Okabe, T. Okabe, F. S. Ohuchi and F. S. Ohuchi, *J. Phys. Chem. C*, 2020, **124**, 12871–12882.
- 61 W. Sun, M. Li, Y. Li, Z. Wu, Y. Sun, S. Lu, Z. Xiao, B. Zhao and K. Sun, *Adv. Theory Simul.*, 2019, **2**, 1–9.
- 62 R. Olivares-Amaya, C. Amador-Bedolla, J. Hachmann, S. Atahan-Evrenk, R. S. Sánchez-Carrera, L. Vogt and A. Aspuru-Guzik, *Energy Environ. Sci.*, 2011, **4**, 4849–4861.
- 63 H. Sahu, F. Yang, X. Ye, J. Ma, W. Fang and H. Ma, *J. Mater. Chem. A*, 2019, **7**, 17480–17488.
- 64 D. Padula, J. D.-D. Simpson and A. Troisi, *Mater. Horiz.*, 2019, **6**, 343–349.
- 65 L. Simine, T. C. Allen and P. J. Rossky, *Proc. Natl. Acad. Sci. U. S. A.*, 2020, **117**, 13945–13948.
- 66 J. F. Joung, M. Han, J. Hwang, M. Jeong, D. H. Choi and S. Park, *JACS Au*, 2021, **1**, 427–438.
- 67 S. Ye, W. Hu, X. Li, J. Zhang, K. Zhong, G. Zhang, Y. Luo, S. Mukamel and J. Jiang, *Proc. Natl. Acad. Sci. U. S. A.*, 2019, **116**, 201821044.
- 68 C. Nantasenamat, C. Isarankura-Na-Ayudhya, N. Tansila, T. Naenna and V. Prachayasittikul, *J. Comput. Chem.*, 2007, **28**, 1275–1289.
- 69 E. J. Beard, G. Sivaraman, Á. Vázquez-Mayagoitia, V. Vishwanath and J. M. Cole, *Sci. Data*, 2019, **6**, 307.
- 70 S. Varghese and S. Das, *J. Phys. Chem. Lett.*, 2011, **2**, 863–873.
- 71 C. L. Donley, J. Zaumseil, J. W. Andreasen, M. M. Nielsen, H. Sirringhaus, R. H. Friend and J. S. Kim, *J. Am. Chem. Soc.*, 2005, **127**, 12890–12899.
- 72 P. J. Brown, D. S. Thomas, A. Köhler, J. S. Wilson, J.-S. Kim, C. M. Ramsdale, H. Sirringhaus and R. H. Friend, *Phys. Rev. B*, 2003, **67**, 064203.
- 73 C. W. Yap, *J. Comput. Chem.*, 2011, **32**, 1466–1474.
- 74 D.-S. Cao, Q.-S. Xu, Q.-N. Hu and Y.-Z. Liang, *Bioinformatics*, 2013, **29**, 1092–1094.
- 75 H. Moriwaki, Y.-S. Tian, N. Kawashita and T. Takagi, *J. Cheminform.*, 2018, **10**, 4.
- 76 RDKit: Open-Source Cheminformatics Software.
- 77 Z. Luo, R. Ma, Y. Xiao, T. Liu, H. Sun, M. Su, Q. Guo, G. Li, W. Gao, Y. Chen, Y. Zou, X. Guo, M. Zhang, X. Lu, H. Yan and C. Yang, *Small*, 2020, **16**, 2001942.



- 78 M. Y. Mehboob, M. Adnan, R. Hussain and Z. Irshad, *Synth. Met.*, 2021, **277**, 116800.
- 79 R. Todeschini, M. Lasagni and E. Marengo, *J. Chemom.*, 1994, **8**, 263–272.
- 80 R. Todeschini and P. Gramatica, *3D QSAR in Drug Design*, Kluwer Academic Publishers, Dordrecht, 1998, pp. 355–380.
- 81 R. Todeschini and P. Gramatica, *Quant. Struct. Relationships*, 1997, **16**, 113–119.
- 82 R. Todeschini and V. Consonni, *Molecular Descriptors for Chemoinformatics*, Wiley, 2nd edn, 2009, vol. 41.
- 83 R. Todeschini and V. Consonni, *Handbook of Molecular Descriptors*, Wiley, 2000.
- 84 C. Bannwarth, E. Caldeweyher, S. Ehlert, A. Hansen, P. Pracht, J. Seibert, S. Spicher and S. Grimme, *Wiley Interdiscip. Rev.: Comput. Mol. Sci.*, 2021, **11**, e1493.
- 85 N. Artrith, K. T. Butler, F.-X. Coudert, S. Han, O. Isayev, A. Jain and A. Walsh, *Nat. Chem.*, 2021, **13**, 505–508.
- 86 M. Lee, *Adv. Energy Mater.*, 2019, 1900891.
- 87 F. Pedregosa, R. Weiss, M. Brucher, G. Varoquaux, A. Gramfort, V. Michel, B. Thirion, O. Grisel, M. Blondel, P. Prettenhofer, R. Weiss, V. Dubourg, J. Vanderplas, A. Passos, D. Cournapeau, M. Brucher, M. Perrot and É. Duchesnay, *J. Mach. Learn. Res.*, 2011, **12**, 2825–2830.
- 88 D. Rogers and M. Hahn, *J. Chem. Inf. Model.*, 2010, **50**, 742–754.
- 89 L. H. Hall and L. B. Kier, *J. Chem. Inf. Comput. Sci.*, 1995, **35**, 1039–1045.
- 90 D. C. Elton, Z. Boukouvalas, M. S. Butrico, M. D. Fuge and P. W. Chung, *Sci. Rep.*, 2018, **8**, 9059.
- 91 C. Bannwarth, S. Ehlert and S. Grimme, *J. Chem. Theory Comput.*, 2019, **15**, 1652–1671.
- 92 S. Grimme, C. Bannwarth and P. Shushkov, *J. Chem. Theory Comput.*, 2017, **13**, 1989–2009.
- 93 F. Deledalle, T. Kirchartz, M. S. Vezie, M. Campoy-Quiles, P. S. Tuladhar, J. Nelson and J. R. Durrant, *Phys. Rev. X*, 2015, **5**, 1–13.
- 94 F. C. Spano, *Acc. Chem. Res.*, 2010, **43**, 429–439.
- 95 G. Forti, A. Nitti, P. Osw, G. Bianchi, R. Po and D. Pasini, *Int. J. Mol. Sci.*, 2020, **21**, 8085.
- 96 L. A.-A. Pettersson, L. S. Roman and O. Inganäs, *J. Appl. Phys.*, 1999, **86**, 487–496.

